UC Davis

UC Davis Previously Published Works

Title

Biofilms in 3D porous media: Delineating the influence of the pore network geometry, flow and mass transfer on biofilm development

Permalink

Authors

Carrel, Maxence
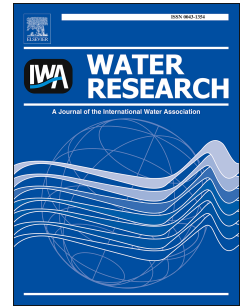Morales, Verónica L
Beltran, Mario A
et al.

Publication Date

DOI

Accepted Manuscript

Biofilms in 3D porous media: Delineating the influence of the pore network geometry, flow and mass transfer on biofilm development

Maxence Carrel, Verónica L. Morales, Mario A. Beltran, Nicolas Derlon, Rolf Kaufmann, Eberhard Morgenroth, Markus Holzner

Please cite this article as: Carrel, M., Morales, Veró.L., Beltran, M.A., Derlon, N., Kaufmann, R., Morgenroth, E., Holzner, M., Biofilms in 3D porous media: Delineating the influence of the pore network geometry, flow and mass transfer on biofilm development, *Water Research* (2018), doi: 10.1016/j.watres.2018.01.059.

Biofilms in 3D porous media: delineating the influence of the pore network geometry, flow and mass transfer on biofilm development

Maxence Carrel[a], Verónica L. Morales[a,b], Mario A. Beltran[c,d], Nicolas Derlon[a,e],
Rolf Kaufmann[d], Eberhard Morgenroth[a,e] and Markus Holzner[a*]

[a] Institute of Environmental Engineering, ETH Zürich, Stefano-Franscini-Platz 5, 8093 Zürich, Switzerland

[b] Department of Civil and Environmental Engineering, University of California, Davis, California, USA

[c] School of Science, RMIT, Melbourne, Australia

[d] Empa, Swiss Federal Laboratories for Materials Science and Technology, Center for X-ray Analytics, Dübendorf, Switzerland

[e] Eawag, Swiss Federal Institute of Aquatic Science and Technology, Dübendorf, Switzerland

Email contact of authors:
holzner@ifu.baug.ethz.ch

[*] Corresponding author

31   **Graphical Abstract**
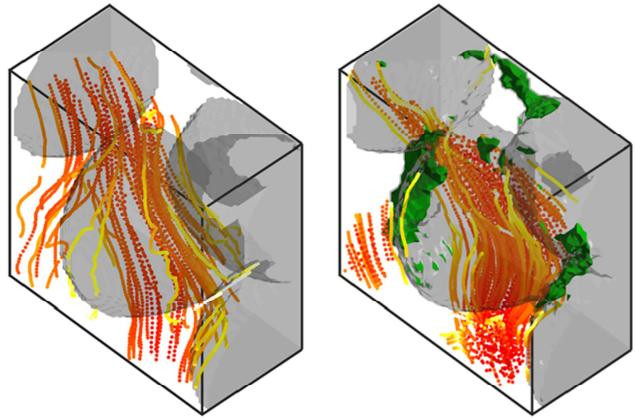
32

Biofilm development in a 3D porous medium

Biofilm adhesion, development and morphology are defined by the local wall shear stress distribution

33

34

35

36

37

Abstract

This study investigates the functional correspondence between porescale hydrodynamics, mass transfer, pore structure and biofilm morphology during progressive biofilm colonization of a porous medium. Hydrodynamics and the structure of both the porous medium and the biofilm are experimentally measured with 3D particle tracking velocimetry and micro X-ray Computed Tomography, respectively. The analysis focuses on data obtained in a clean porous medium after 36 h of biofilm growth. Registration of the particle tracking and X-ray data sets allows to delineate the interplay between porous medium geometry, hydrodynamic and mass transfer processes on the morphology of the developing biofilm. A local analysis revealed wide distributions of wall shear stresses and concentration boundary layer thicknesses. The spatial distribution of the biofilm patches uncovered that the wall shear stresses controlled the biofilm development. Neither external nor internal mass transfer limitations were noticeable in the considered system, consistent with the excess supply of nutrient and electron acceptors. The wall shear stress remained constant in the vicinity of the biofilm but increased substantially elsewhere.

1 Introduction

Biofilms are communities of bacteria attaching and developing on surfaces embedded in a matrix of extracellular polymeric substances (EPS) and persistently developing in environmental, medical and industrial settings. In porous media such as soils, many prokaryotic microorganisms develop a sessile lifestyle that allows them to better cope with their environment (Griebler and Lueders 2009). As biofilms are ubiquitous in porous media systems, their relevance stretches over a wide range of applications spanning from the bioremediation of contaminated aquifers (Meckenstock et al. 2015), fixed bed trickling filters (Gujer and Boller 1986, Morgenroth et al. 1996, Gülay et al. 2014) or membrane filtration systems (Baker and Dudley 1998). For all these different applications, biofilm formation can have a positive or detrimental impact. Therefore understanding biofilm development in respect to the local geometry of the pore network, the porescale hydrodynamics and mass transfer processes is a prerequisite for optimal biofilm control. The investigation of these processes requires access to wall shear stresses and concentration boundary layer distributions (Eberl et al. 2000, Picioreanu et al. 2000) based on locally resolved flow and structural information.

The development of biofilms in porous media is a process involving a wide range of scales, from micro- over meso- to macroscale (Battin et al. 2007). For instance, microscale hydrodynamics were shown to control the initial attachment of individual bacteria or particulate matter to surfaces (Rusconi et al. 2014, Radu et al. 2014). The macroscale is the scale relevant for the integrated understanding of larger engineering or natural systems (e.g., reactors, aquifers). The mesoscale links the micro- and the macroscale, as it is the scale at which flow and mass transfer interact with and define the biofilm structures (Eberl et al. 2000). The focus of this study is the mesoscale in porous media or porescale. The processes that drive growth of biofilms are complicated by the complexity of the pore space in which

84 they grow in natural porous media, and by the feedback mechanisms between pore clogging

85 from biofilm growth and solute transport (to deliver nutrients and carry away wastes). Subtle

86 changes to the pore structure have been reported to affect pore velocities and characteristic

87 length scales (i.e. pore radii) by orders of magnitude (Seymour et al. 2004, Holzner et al.

88 2015). Porous media can be considered as networks of connected three-dimensional

89 roughness elements or corners representative of e.g. soils or filters but also of many other

90 pore-scale environments in which biofilms develop.

91 Biofilm development in porous structures result from highly diverse and complex phenomena.

92 For instance, the growth of biofilms was identified to induce the formation of preferential

93 flow paths, while the interplay between biofilm growth, detachment, decay and lysis was

94 numerically shown to cause the intermittent shifting of these flow paths (Bottero et al. 2013).

95 Locally, the intricate geometry of the pore network and the evolving flow field during biofilm

96 growth influence competition between bacterial communities, as slow growing or non-EPS-

97 producing bacteria can outcompete fast growing or EPS-producing ones (Coyte et al. 2017,

98 Nadell et al. 2017). Various studies of biofilm formation at the porescale mainly considered

99 porous media with two-dimensional pore-networks either experimentally (Drescher et al.

100 2013, Qian et al. 2017) or numerically (Kapellos et al. 2007). The use of new imaging

101 methods such as Optical Coherence Tomography (OCT) allows linking biofilm formation to

102 local hydrodynamic conditions and overall system performances (Xi et al. 2006, Wagner et al.

103 2010a, Derlon et al. 2012). OCT allows imaging the biofilm physical structure at the meso-

104 scale. But OCT can also be combined with fluid flow modeling to study flow dynamics (Gao

105 et al. 2014, Weiss et al. 2015). However, the penetration depth of the OCT's signal is limited

106 to around 2 mm in biofilms, which restrains the application of OCT for monitoring biofilm

107 formation in 3D porous media. Another relevant method is magnetic resonance imaging

108 (MRI). MRI has been used to investigate transport processes in progressively bioclogged 3D

109   porous media at the pore (Seymour et al. 2004) and at the Darcy scale (Codd et al. 2011).

110   Wagner et al. (2010b) used MRI to study the link between the biofilm formation in a tubular

111   reactor and its influence on the 3D velocity distribution. Results from MRI imaging revealed

112   that biofilm patches could resist maximum local shear stresses up to seven times higher than

113   the mean ones. However, several aspects limit a wide application of MRI to study of biofilm

114   formation in porous media: access to device, cost of the apparatus and use of dedicated flow-

115   cells adapted to the MRI, etc. Despite recent progresses, the availability of experimental

116   methods to provide information about both the porescale flow and biofilm development in

117   fully 3D porous media remains limited.

118   Experimental data on porescale biofilm properties and hydrodynamics are also required to

119   validate numerical models developed to predict biofilm formation in porous media. A

120   parameter of interest is the biofilm shear strength—the resistance of biofilms to shear exerted

121   by the surrounding fluid. The biofilm shear strength is experimentally challenging to measure

122   and vary with the growth conditions and bacterial type. Yet, many models often use a default

123   value of the biofilms shear strength that may not be representative of their biofilms, thus

124   highlighting the need for direct measurements of biofilm shear strength in 3D porous media.

125   This is reinforced by the wide distributions of biofilm shear strengths mentioned in recent

126   studies (e.g. Stewart (2014)), which can be attributed to the natural heterogeneous distribution

127   of material properties of biofilms (Stewart and Franklin 2008), but also to the distribution of

128   wall shear stresses exerted by fluid flow on biofilms as a consequence of velocity gradients in

129   the biofilm vicinity (Stewart 2014). Additionally, the wall shear stresses exerted on the

130   biofilm are very often roughly approximated based on the initial hydrodynamic conditions

131   (Derlon et al. 2008, Blauert et al. 2015), thus not accounting for the effect of the biofilm

132   formation on the flow, which increases the uncertainty of the assumed biofilm shear strength.

6

133 The goal of this paper is thus to experimentally investigate the influence of porescale

134 hydrodynamics and mass transfer processes (specifically, wall shear stress and concentration

135 boundary layer distribution functions) on biofilm development in a transparent 3D porous

136 media. A biofilm was grown in a 3D porous medium for 36 hours under a constant volumetric

137 flow rate with nutrients and electron acceptors supplied in excess. The hydrodynamics were

138 measured at the porescale with three-dimensional particle tracking velocimetry (3D-PTV) in a

139 clean porous medium and after biofilm growth. The structure of the porous medium, along

140 with the morphology and spatial distribution of the biofilm were obtained with X-ray micro

141 Computed Tomography (X-ray μCT). The novel combination of hydrodynamic and structural

142 data permit direct measurements of the feedback mechanisms between biofilm patch

143 development and the fluid dynamics at the porescale to answer the following research

144 questions:

145 • How does the growth of the biofilm depend on the local wall shear stress and local

146 mass transfer processes?

147 • What is the influence of the growing biofilm on the porescale hydrodynamics (pore-

148 scale velocities, wall shear stresses and concentration boundary layer thicknesses)?

2. Material and Methods

149

150 2.1 Porous medium

151 The porous medium used in this work consists of Nafion pellets (Ion Power, Munich,

152 Germany), a material with physico-chemical properties similar to that of sand grains (Downie

153 et al. 2012). The diameter d_N of the pellets is roughly monodisperse and distributed around 2.5

154 ± 0.5 mm. Nafion is an iono-polymer whose optical refractive index can easily be matched

155 (RIM) with aqueous solutions yielding models of transparent soil (Downie et al. 2012). Here,

156 a decent RIM was obtained with a glucose concentration of 11 % w/v (see Supplementary

7

157 Information 1 for a detailed analysis concerning the refractive index matching optimization).

158 The Nafion pellets underwent three times the following treatment allowing optimal

159 transparency. Approximately 20 g. of pellets were heated up at 65°C for 1 h while stirred at

160 200 rpm under reflux. Afterwards the pellets were cooled for 30 min at room temperature and

161 stored overnight at 4°C.

2.2 Biofilm cultivation

163 The 11% w/v glucose solution used as a growth medium in this study was prepared with tap

164 water. In order to enhance the growth of the heterotrophic biofilm cultivated in this

165 experiment, nitrogen and phosphorus were added to a molar ratio C:N:P of 1000:1:1. This low

166 ratio is due to the high glucose concentration that was not only serving as a carbon source but

167 also provided the refractive index matching with the Nafion grains. Nitrate ($NaNO_3$) was here

168 serving both as nitrogen source and electron acceptor. Phosphorus was added as K_2HPO_4 and

169 $NaH_2PO_4 \cdot 2H_2O$ accounting for 1/3 and 2/3, respectively, of the total phosphorus molecular

170 ratio, yielding inflow concentrations of 8.14 mg NO_3^--N/L and 18.9 mg PO_4^{3-}-P/L.

171 The mixed species bacterial inoculum used in this study was isolated from the Chriesbach

172 River (Dübendorf, Switzerland, Desmond et al. (2018)). The frozen bacterial inoculum

173 contained in (2 mL) Eppendorf tubes was added to 100 mL of the growth medium. It was then

174 incubated for 20-24 h at 30°C and stirred at 200 rpm until reaching midlogarithmic phase

175 (OD_{600} 0.52 ± 0.096). The incubation procedure was repeated three consecutive times for the

176 bacteria to adapt to the synthetic carbon source of the growth medium. For the last incubation

177 cycle, the Nafion grains were added to the growth medium to allow initial bacterial

178 attachment. Upon the incubation, a custom built PMMA flow-cell ($38 \times 38 \times 16$ mm^3) was

179 wet packed with the inoculated Nafion grains. Bottles containing 10 L of growth medium

180 were connected to the flow cell with silicon tubing (VWR, Dietikon, Switzerland) previously

181 washed with 70% v/v ethanol and thoroughly rinsed with deionized water. The growth

8

182   medium was replaced every 12 h and spiked with 100 mL of the inoculum. A peristaltic pump

183   (Ismatec, Glattbrugg, Switzerland) was used to set a volumetric flow rate of 10 mL/min. As

184   illustrated in Figure 1 (a), a syringe was used as a bubble trap as well as to dampen the

185   pulsatile flow created by the peristaltic pump. Nitrate and oxygen concentration were sampled

186   in the effluent every 12 hours and revealed a high bacterial activity but no actual nutrient

187   limitations (4.41 ± 0.67 mg NO_3^--N/L and 4.84 ± 0.55 mg O_2/L respectively).

188   **Figure 1**

189   ## 2.3 Three-Dimensional Particle Tracking Velocimetry

190   The three-dimensional particle tracking velocimetry (3D-PTV) method applied in this work

191   allows for detection and tracking of flow particle tracers, which move faithfully with the

192   porewater. Tracking the position of tracer particles provides data on velocity and acceleration

193   along flow trajectories. This method was developed to study turbulent flows (Hoyer et al.

194   2005) and was lately adapted to study flows in porous media (Holzner et al. 2015). In order to

195   perform 3D-PTV measurements, the flow cell was connected to a 120 mL syringe mounted on

196   a syringe pump (Lambda Vit-Fit, Lambda, Baar, Switzerland). The volumetric flow rate was

197   set to 10 mL/min, yielding a Darcy velocity q of 0.27 mm/s. The estimated Reynolds number

198   was $Re = q\, d_N/\nu \approx 0.5$, where ν is the kinematic viscosity of the glucose aqueous solution ($\nu =$

199     $1.33\ e^{-6}$ m^2/s at 20 °C). The tracer particles were composed of fluorescent Red Polyethylene

200   Microspheres (Cospheric, Santa Barbara, CA USA) with a density of 1 g/cm^3 and with a

201   diameter d_P of ca. 70 µm (> 90 % between 63 and 75 µm) were added to the growth medium

202   to create a suspension. As these particles are neutrally buoyant, inertial effects are not of

203   concern and the particles follow the flow reliably (Holzner et al. 2015).

204   For each 3D-PTV measurement, the tracer particle concentration added is of 0.02 g/L,

205   corresponding to a volume fraction of 0.002%, which is low enough to ensure that particle-

206   particle interactions were not of concern. The fluorescent tracer particles were illuminated

9

207 with a 100 W pulsed Nd:YLF laser ($\lambda = 527$ nm, Darwin Duo, Quantronix, Hamden, USA).

208 Figure 1 (b) shows the setup used for the 3D-PTV experiments. The flow cell was imaged

209 from both the front and back sides with a Photron Fastcam SA5 with a resolution of

210 1024×1024 at 50 frames per second (fps) using an image splitter providing 4 stereoscopic

211 views. Between 30 and 200 particles were tracked per frame, yielding ca. 10^6 data points for

212 every measurement (4549 and 4193 trajectories for the time points $T = 0$ and $T = 36$ h

213 respectively) and 3D particle locations with an accuracy of ca. 50 µm (Holzner et al. 2015).

214 Assuming stationarity of the porescale flow and neglecting structural changes induced by

215 biofilm growth during 3D-PTV experiments (ca. 30 min), an estimated average inter-particle

216 distance of ca. 50 µm was obtained. Additional information about processing of the 3D-PTV

217 data and extraction of the wall shear stresses is available in the Supplementary Information 2.

218 2.4 X-ray micro-tomography

219 Biofilms form porous structures (up to 90 % porosity) (Wagner et al. 2010a) with high water

220 content and densities very close to that of water. Thus, the application of X-ray micro-

221 tomography to biofilm imaging requires the addition of contrast agents. Here, we follow the

222 approach presented by Davit et al. (2011) and use a suspension of 0.05 g/mL barium sulfate

223 ($BaSO_4$) particles (Micropaque, Guerbet, Zürich, Switzerland) as a contrast agent that

224 emphasizes the porespace free of biofilm. Davit et al. (2011) noted the occurrence of biofilm

225 detachment occurring during the $BaSO_4$ injection. Carrel et al. (2017) suggested to use iron

226 sulfate ($FeSO_4$) as a contrast agent by continuously adding it to the biofilm during culturing

227 and thus avoiding detachment. However, this approach could not be applied here without

228 negatively affecting the RIM. Therefore, $BaSO_4$ was used as a contrast agent. In order to

229 minimize biofilm-contrast agent interactions, the injection of the $BaSO_4$ was done over 12 h at

230 a volumetric flow rate 500 times smaller than the growth flow rate.

231 X-ray μCT scans of the biofilm samples were performed at the Swiss Federal Laboratories for

232 Materials Science and Technology (EMPA, Dübendorf, Switzerland) on a custom-built

233 scanner equipped with a tungsten microfocus source with cone-beam configuration and a 40 x

234 40 cm^2 flat panel detector. Four frames of 1441 projections were acquired over 3 hours at a

235 voltage of 80 kV and focused electron beam current of 125 μA. Reconstruction was

236 performed as presented in Carrel et al. (2017). The resolution of the obtained tomograms was

237 of 27 μm. A first scan was imaged prior to the injection of the contrast agent, in order to

238 obtain the structure of the initial porous media. A second scan was imaged after the injection

239 of the contrast agent in order to obtain the biofilm coated porous media.

240 The reconstructed tomograms exhibited beam-hardening artifacts which were attributed to the

241 polychromatic nature of X-rays, the high absorption coefficient of Barium and the non-

242 homogeneous distribution of the contrast agent within it. These artifacts were mostly localized

243 near the outermost sides of the anisotropic flow cell. Therefore, a central region of sufficient

244 visualization quality was cropped and used for structural analysis, where the artifacts were

245 weaker (with dimensions of $20 \times 20 \times 16$ mm, i.e. 25% of the total flow cell volume).

246 Contrast enhancement of the different materials in the tomographic image was effectuated

247 using FIJI (Schindelin et al. 2012). A non-local mean filter was then run in Avizo (Thermo

248 Fisher Scientific, Hillsboro, Oregon, USA) to improve the signal to noise ratio. Segmentation

249 was done using Avizo and consisted of watershed segmentation refined with morphological

250 operations (closing of the solid grains and the biofilm as well as opening of the air bubbles).

251 The air bubbles that entered the flow cell during the injection of the contrast agent were

252 assigned to the liquid phase. Objects smaller than 10 voxels were discarded before the final

253 data evaluation. The procedure presented in Pérez-Reche et al. (2012) was used to measure

254 pore radii along the skeleton of the void space (Additional information concerning the image

255 segmentation is available in the Supplementary Information 3). Bounding boxes fitted to the

11

256 segmented biofilm patches allowed to extract geometric features of the patches such as their

257 aspect ratio, which was obtained by dividing the largest axis of the bounding box by its

258 smallest axis.

259 2.5 Registration

260 The X-ray segmented data set and the 3D-PTV trajectories were registered (e.g. transformed

261 into one coordinate system) in order to allow a local investigation of the biofilm - flow

262 coupling. The registration was performed using a custom registration algorithm. In a first step,

263 the Lagrangian 3D-PTV flow information was mapped on a Eulerian grid of 81 µm size,

264 corresponding to three times the resolution of the X-ray data. The resolution of the X-ray

265 tomograms (27 µm pixels) was decreased accordingly for the ease of calculation (binning

266 based on voxel averages). Consecutively, a linear transformation was obtained by a discrete

267 pseudo - digital volume correlation maximizing the following criterion:

$$r_{ijl} = \frac{\sum_m \sum_n \sum_o [V_X(m+i, n+j, o+l)][V_P(m,n,o)]}{\sum_m \sum_n \sum_o [V_P(m,n,o)]}$$

268 where i, j, and l are the components of the displacement vector $D(i,j,l)$, V_X is the segmented

269 liquid phase of the volumetric X-ray data set and V_P is the amount of 3D-PTV Lagrangian

270 data mapped on the Eulerian grid. The final r_{ijl} obtained for the different data sets were of

271 88.67% for the clean porous media and of 76.78% for the bioclogged packing. The

272 uncertainty related to the registration can be inferred to partial volume effects due to the

273 decreased resolution of the tomograms and to the accuracy of the 3D-PTV. Figure 2 (a-d)

274 allows assessing the quality of the registration.

275   **Figure 2**

276

12

277 ## 2.5 Calculation of local wall shear stress and concentration boundary layer

278 ## thickness

279 The registered data provided the basis for a local analysis of hydrodynamic and mass transfer

280 processes. A first variable of interest is the wall shear stress τ_w, defined as $\tau_w = \mu \frac{\partial v}{\partial n}$ where μ

281 is the dynamic viscosity of the fluid and $\frac{\partial v}{\partial n}$ the velocity gradient defined by the velocity

282 magnitude v and the vector n normal to the triangulated faces of the solid phase (Nafion

283 grains) or to the biofilm surface ($|n| = 0$). In order to evaluate this velocity gradient, the

284 Lagrangian data was first binned on an Eulerian grid of 100 µm mesh size. As the

285 interparticle distance of the 3D-PTV data was of ca. 50 µm on average, the Eulerian velocity

286 field obtained after binning was not perfectly filled, i.e. there were empty voxels which were

287 not sampled by any fluid particle. The velocity gradients were then interpolated linearly from

288 the Eulerian velocity field on the normal of the solid surface (Nafion grains or biofilm)—that

289 is for all surface patches where velocity information was available—thus providing access to

290 the wall shear stress distribution. Velocity profiles within pores typically exhibit parabolic

291 profiles (de Anna et al. 2017). The accuracy for the wall shear stress was estimated at 8% by

292 comparing both a linear and a quadratic interpolation of the velocity profile to obtain two

293 different approaches for determining wall shear stress. The comparison between the two

294 interpolation methods indicates that the spatial resolution of the velocity map was sufficient to

295 retrieve wall shear stress with satisfying accuracy. Note that τ_w was approximated assuming a

296 no-slip boundary condition at the biofilm surface and thus, non-permeable biofilms. However,

297 several authors showed that biofilms are permeable and have networks of submicroscopic

298 channels (Davit et al. 2013, Stoodley et al. 1994). Since the permeability of biofilms is

299 generally fairly low (Deng et al. 2013), we infer that its influence on the approximation of the

300 wall shear stresses is negligible. A second variable of interest that allows assessment of the

301 interplay of mass transfer conditions on biofilm development is the concentration boundary

302   layer thickness δ_c. The mass transfer coefficient $k_s = D_s/\delta_c$ indicates the rate at which

303   substrate or electron acceptors diffuse over the concentration boundary layer thickness δ_c from

304   the bulk of the pore network towards the surface of the grain. Therefore, nutrient limitations

305   are less prone to occur for small concentration boundary layer thicknesses. In order to

306   estimate δ_c, we firstly consider that it is linked to the hydraulic boundary layer thickness δ_v as

307   $\delta_c = \delta_v/Sc^{1/3}$, where the Schmidt number $Sc = v/D$ expresses the ratio of momentum

308   diffusivity (v) to mass diffusivity (D). The thicknesses δ_c and δ_v are commonly defined as

309   lengths stretching normally from the substratum to the 99th percentile of fully developed

310   concentration or velocity profiles respectively. Here, due to the intricate substratum

311   geometries and velocity profiles, the hydraulic boundary layer thickness δ_v is approximated by

312   considering the length scale associated with molecular diffusion of momentum as induced by

313   shear as $\delta_v = \sqrt{v/\frac{\partial v}{\partial n}}$. This means that the concentration boundary layer thickness δ_C is

314   proportional to $\tau_w^{-1/2}$. Strictly, at locations with negligible biofilm the boundary layer

315   thickness should be very small because no appreciable substratum gradient is present. This

316   implies that using this approach we likely overestimate δ_C in such locations. In the

317   comparative analysis below, we are interested in the dominant factors that control biofilm

318   growth. Hence, our approach provides an estimate of the local δ_C that will develop after

319   biofilm has grown in a given location.

3. Results

321   3.1 Registered data

322   Figure 2 presents the results of the registered 3D-PTV and X-ray data for the central region of

323   the flow cell for the initial clean porous medium (T = 0 h) in (a) and after 36 h of biofilm

324   development in (b). Figure 2 (c) and (d) are local close-ups of (a) and (b). The tracer particle

325   trajectories in Figure 2 are color-coded with the velocity magnitude, illustrating the

326 intermittency of velocities along trajectories typical of porous media flows (de Anna et al.

327 2013). The increasingly darker coding of the velocities along trajectories reflects the average

328 velocity increase. Additionally, biofilm growth induced substantial changes on the flow field

329 (compare Figure 2 (a) and (b)), which is restricted to fewer channels.

330 In Figure 2 (b) biofilm patches are distributed in between Nafion grains. Note that in Figure 2

331 (b), the flow information is not distributed homogeneously. This could either be caused by

332 flow tracers not sampling stagnation zones or because the view of the particles was obstructed

333 by biofilm patches. The close-ups in Figure 2 (c) and (d) show local changes of the flow field

334 upon biofilm growth. The biofilm patches illustrated in Figure 2 (d) exhibit a high aspect ratio

335 and an orientation approximately aligned with the initial flow direction. Upon biofilm growth,

336 the channel on the left of the central grain presented in Figure 2 (d) appears to be clogged,

337 indicating that growth of a biofilm patch in a pore results in local obstruction of the flow,

338 which consequently is compensated by significant hydrodynamic changes. Figure 2 (e) and (f)

339 present triangulated meshes of the biofilm patches presented in the close-ups and bounding

340 boxes fitted to each individual patch to extract biofilm size and aspect ratio.

341 ## 3.2 Influence of biofilm growth on porescale statistics

342 In order to quantify the influence of biofilm growth on the porescale hydrodynamics, we

343 conduct a statistical analysis on relevant variables such as the distributions of average

344 porescale velocities, pore radii, wall shear stresses, and concentration boundary layer

345 thicknesses in the clean and bioclogged porous medium. Figure 3 presents the probability

346 density functions (PDFs), which can be considered normalized continuous histograms for the

347 listed variables in the presence and absence of biofilm. Figure 3 (a) presents the PDF of the

348 velocity magnitude for the clean and bioclogged porous medium. Upon biofilm growth, there

349 is a slight increase of the average velocity and a substantial increase of the variance, as seen in

350 the greater frequency in low and high velocities (heavy PDF tailing). These increased tailings

351 are typical of flow fields for pore networks of increasing heterogeneity (Morales et al. 2017,

352 Siena et al. 2014). This indicates that the growing biofilm affects the pore structure and leads

353 to the formation of preferential flow paths (increased velocity tails) and slow velocity zones

354 (increased low velocity tail of the PDF). The impact of the biofilm on the pore structure is

355 further confirmed by Figure 3 (b) showing the pore radii distribution for the clean and

356 bioclogged packings. With biofilm growth, the average pore radius decreases from 0.41 mm

357 to 0.33 mm. Note that these distributions have an exponential tail typical of pore radii

358 distribution in porous media (Holzner et al. 2015).

359   **Figure 3**

360 The wall shear stress distributions obtained are presented in Figure 3 (c) and span a range of

361 over two orders of magnitude. With biofilm growth, the pore space is reduced and average

362 velocity increased due to mass conservation, while the wall shear stresses increase

363 substantially. Figure 3 (d) shows the distribution of the concentration boundary layer

364 thicknesses δ_c for the clean and bioclogged porous media. As a consequence of the wall shear

365 stress increase observed previously, the concentration boundary layer thickness decreases

366 accordingly.

367 3.3 Local statistical analysis

368 In this section, we consider the distributions of variables describing the geometry of the pore

369 network and the local hydrodynamics presented in Figure 3. Of interest is the investigation of

370 how these variables locally influence the biofilm or are themselves changed by the developing

371 biofilm. We consider all the points of pore network's skeleton (see Figure 2c) and investigate

372 whether biofilm patches develop in their vicinity (within a distance of one pore radius). This

373 allows us to understand how locally flow and mass transfer influence biofilm development.

374 For the initial time point (at 0 hrs of biofilm growth), this distinction is performed with

375 hindsight for Nafion faces on which biofilm will develop (BF,0) or those on which it will not

16

376   (N,0). For the bioclogged data (at 36 hrs of biofilm growth), the distinction is made by

377   classifying surfaces with observable biofilm development (BF,36) or Nafion grain surfaces

378   that remained uncolonized (N,36).

379   **Figure 4**

380   Figure 4 (a) and (b) show the PDFs of the porescale velocity magnitude in the vicinity of the

381   developing biofilm (BF) and on uncolonized channels (N) before and after biofilm growth.

382   The PDFs do not show appreciable differences, indicating that the porescale velocities do not

383   directly influence the biofilm development. Figure 4 (c) and (d) show a similar comparison

384   for the pore radii before and after biofilm growth. Here, a noticeable difference emerges, as

385   the pore radii where the biofilm initially develops are on average smaller than in channels

386   where no biofilm grows. Additionally, the pore radii in the biofilm vicinity after 36 h of

387   growth show a substantial shift in distribution (see Figure 4, d) toward smaller overall pores,

388   particularly in the vicinity of the biofilm. This suggests an increase of the biofilm specific

389   surface area, which is a key parameter for the estimation of mass transfer characteristics

390   within biofilms (Horn and Lackner 2014).

391   **Figure 5**

392   The distributions of the wall shear stress values obtained for the surface of the clean Nafion

393   grains (solid lines) and for the surface of the nascent biofilm (dashed lines) are shown in

394   Figure 5 at a time prior to biofilm growth (a) and after biofilm growth (b). Although the

395   distribution of wall shear stresses is wide with and without biofilm presence, a strong

396   difference between the two types of surfaces is noticeable. From these data it is possible to

397   note that the maximal wall shear stress for the surfaces that will not be colonized by the

398   biofilm are about twice as large as those where nascent biofilm is found at 36 hr. Substantial

399   differences are also observed for the concentration boundary layer thicknesses depicted in

400   Figure 5 (c) and (d). No biofilms were observed to colonize or develop in the high wall shear

17

401   stress regions, despite the small concentration boundary layers present there, corroborating

402   that wall shear stress controls biofilm development in the present experiment. We conjecture

403   from these data that too small pores do have sufficient flux of nutrients to sustain biofilm

404   growth. Mainly, diffusion is the mechanism for nutrient mass transfer, which can be limiting.

405   Too large pores experience high shear, which we interpret to be hydrodynamically

406   unfavourable for biofilms to become established. Presumably the high wall shear detaches

407   nascent colonies and thus prevents significant EPS from developing.

408   3.4 Morphology of the biofilm patches

409   Figure 6 (a) shows the PDF of the biofilm patch size which follows a power law distribution,

410   where the probability approximately decreases with the inverse of the size. Figure 6 (b) shows

411   the correlation of biofilm patch sizes with average pore radii of the clean porous medium in

412   which the patches grew over the course of the experiment. The biofilm patch size increases

413   with the pore radii, which is expected since the biofilm patches are confined by the radii. The

414   largest biofilm patches are found for average radii of 0.47 mm, slightly larger than the average

415   radius of the porous medium ($\langle r_P \rangle = 0.41$ mm, where the angular brackets denote an average

416   performed over all measured radii). The largest radii appear to be associated with rather small

417   biofilm patches. The wide distribution of the biofilm patch sizes indicates that there is no

418   simple direct relation between the patch size and the pore radii. Figure 6 (c) shows the PDF of

419   the biofilm patches aspect ratio, which is widely distributed and displays a rather high average

420   indicating that elongated shapes are not atypical. Figure 6 (d) shows the correlation of biofilm

421   patch size to aspect ratio, indicating that the maximal size of the biofilm patches decreases

422   with increasing aspect ratio. The PDF of the biofilm thickness, defined as the distance

423   between the biofilm faces to the closest grain faces, is presented in Figure 6 (e). The wide

424   range of biofilm thicknesses observed reflects the patchiness of the biofilm morphologies

425   visible in Figure 3 (e) and (f). Finally, Figure 6 (f) depicts the correlation of biofilm thickness

426 with initial wall shear stress, showing that the maximal biofilm thickness tends to decrease

427 with increasing wall shear stresses.

428 **Figure 6**

429 3.5 Relation between porescale velocities and radii

430 Figure 7 shows joint PDFs of the normalized velocity and of the normalized pore radius for

431 the clean porous medium (a) and the bioclogged medium (b). Holzner et al. (Holzner et al.

432 2015) conjectured the dependence of the maximum porescale velocity v_m on the pore radius r_P

433 according to the power law:

$$v_m = v_0(r_P/r_0)^\alpha, \qquad -2 \leq \alpha \leq 2$$

434 where v_0 and r_0 represent characteristic velocities and pore radii. The exponent α is a

435 parameter reflecting the pore network geometry and stretches from -2 for a completely serial

436 pore arrangement (few pathways through which water can flow) to 2 for a completely parallel

437 one (many equally probably pathways for water to flow). The limits to this power law scaling

438 are indicated in Figure 7 as a dashed-dotted and a dashed line. The white circles show the

439 conditional average of $v/<v>$ on $r_P/<r_P>$ and the continuous line shows a power law fitted to

440 the conditional average. The fitted exponent is noted as imbedded text in the figures. The

441 width of the joint PDFs of $v/\langle v \rangle$ and $r_P/\langle r_P \rangle$ increases with biofilm growth, but are found

442 within the scaling corresponding to completely parallel or serial pore arrangements. The

443 exponents measured decrease from 0.257 to 0.063, reflecting how the pore arrangement

444 changes from parallel towards more serial with biofilm growth.

445 **Figure 7**

4. Discussion

4.1 How does the growth of the biofilm depend on the local wall shear stress and local mass transfer processes?

The overarching goal of this study is to provide experimental evidence allowing to delineate the influence of porous medium geometry, flow and mass transfer processes on the formation of biofilms in a 3D porous medium. The results obtained indicate that, in 3D porous media representative of some natural and engineering systems, biofilms are exposed to wide distributions of wall shear stresses and concentration boundary layer thicknesses. Biofilm especially tends to develop in low wall shear stress regions (Figure 5 (a) and (b)). After 36 h of growth, results from X-ray µCT and 3D-PTV revealed that biofilm formation occurred in the regions of low shear stresses, while no or very low biofilm formation was observed in the regions of high shear stresses. Conversely, mass transfer did not seem to play any role, consistent with presence of nutrient and electron acceptors in excess. Had mass transfer been a key variable, we would expect less biofilm to develop in the regions where the concentration boundary layer is thick (see Figure 5 (c) and (d)). It is important to note that this differs, but does not conflict with, studies on bacteria adhesion to clean surfaces, which are found to preferentially accumulate in high shear regions (Rusconi et al., 2014). Those studies focus on the initial adhesion of biofilm forming cells, while the current work concentrates on biofilm development of uniformly attached cells on all grains surfaces, which we observe is shaped by the local hydrodynamics.

The average of the wall shear stress distributions presented in Figure 5 (a) and (b) in the vicinity of the biofilm and at the surface of the bare grains shows a ca. 1.8 fold increase over the course of the experiment (see Table 1). The increase of the maximal wall shear stress measured is substantially higher (2.5) for the bare grains than at the biofilm surface (1.4). Differences in the increase of the maximal values measured for the biofilm compared to the

471   bare grains suggests that there is a threshold shear stress in the system that the biofilm cannot

472   withstand. This would imply a biofilm shear or cohesive strength of ca. 0.02 N/m^2, which is

473   on the lower end of biofilm shear strengths observed experimentally elsewhere (Stewart

474   2014).

475   **Table 1**

476   The largest biofilm patch sizes were found in pores of radii close to the average radii, but the

477   wide distribution observed for the patch sizes did not indicate that the local geometry of the

478   pore network was substantially influencing biofilm development. The maximal thickness of

479   the biofilm patches decreased with increasing wall shear stress, showing that for the given

480   porous medium and under the present growth conditions, the wall shear stress played a

481   predominant role on controlling biofilm development.

482   4.2 What is the influence of the growing biofilm on the porescale

483   hydrodynamics

484   The prevalence of low wall shear stresses in the vicinity of the biofilms could be attributed to

485   the impact of the growing biofilm on the porescale hydrodynamics. Coyte et al. (2017)

486   showed that the local development of a tiny biofilm patch induced an additional pressure drop

487   at a given location of the pore network, which resulted in substantial non-local changes in the

488   overall flow field. In the present study, the flow rate was kept constant over the course of the

489   experiment. Invoking mass conservation and assuming that the biofilm is homogeneously

490   distributed over a typical cylindrical pore (Thullner and Baveye 2008) would mean that the

491   average velocity would increase in an inverse quadratic relation relative to the pore radius

492   ($v \propto Q/(\pi r^2)$) (see dashed-dotted lines on Figure 7). However, as the data presented in this

493   study show, the biofilm is not homogeneously distributed at the grain surface. Furthermore,

494   even if the flow rate were kept constant such that the pressure gradient increased at the flow

495   cell scale, locally, it is possible to have zones with only small pressure gradient variations. For

21

496 similar pressure gradients, according to Poiseuille's law, the velocity is proportional to the

497 square of the radius ($v \propto r^2$ see dashed lines on Figure 7), so that low velocity regions or

498 stagnant zones can form with biofilm growth. These considerations suggest that predicting the

499 local impact of the growth of biofilm on the porescale hydrodynamics is far from trivial, as

500 for example, porescale velocities could increase or decrease with the pore radius variation.

501 The complex interactions between biofilm development and porescale hydrodynamics is

502 illustrated by the radius-velocity relation presented in Figure 7. The experimental data

503 presented in this study shows that there is a formation of high velocity regions, as also

504 indicated by the high velocity tails of the velocity magnitude PDFs (Figure 3 a).

4.3 Significance

506 To our knowledge, our work is one of the first experimental studies of the biofilm shear

507 strength in three-dimensional porous media. It is important to note that the small wall shear

508 stress values obtained here are of the same order of magnitude than values obtained elsewhere

509 for low Reynolds number flows (Nadell et al. 2017, Song et al. 2014). If we consider

510 variability in shear strengths from different types of biofilms, the direct measurements of wall

511 shear strength presented here are on the lower end of values reported in other studies (0.1 to

512 more than 10'000 N/m^2 as reported in Möhle et al. (2007), Derlon et al. (2008) or Stewart

513 (2014)). The ability of measuring in-situ the biofilm shear strength in 3D porous media opens

514 several research opportunities, namely to use this approach for the validation of numerical

515 models.

516 Numerical models often rely on default values of biofilm shear strengths obtained from the

517 literature (Bottero et al. 2013, Pintelon et al. 2012). Our results, however, underline the risk

518 associated with using generic values for the biofilm shear strength, because these values

519 might relate to non-relevant growth conditions and thus overestimate this system parameter.

22

520   The experimental method introduced in our study allows to access realistic biofilm shear

521   strengths in 3D porous media with an accuracy of about 8%. We suggest that this approach

522   can hence be used to validate assumptions made for numerical models of biofilm formation in

523   3D porous media providing distributions of wall shear stress values local to the biofilm.

524   Given that both optical camera setups and laboratory X-ray scanners become more and more a

525   standard equipment of many laboratories, our approach offers a viable method to resolve the

526   geometry of the porous media in conjunction with the biofilm morphology as well as

527   distribution of the local wall shear stresses. A limitation of our method is that the X-rays

528   might inactivate cells of the biofilm, which would impact subsequent measurements of

529   biofilm morphology. In this study, we have analyzed only one bioclogged state (T=36 h) and

530   we have not quantified this possible influence, which therefore remains a subject of future

531   work. Possible alternative methods, which would not suffer from this limitation, are based on

532   magnetic resonance microscopy adapting the approach introduced by (Wagner et al. 2010b) to

533   3D porous media or by combining 3D geometries obtained from X-ray micro-tomography

534   with numerical studies of coupled flow and biofilm growth (Peszynska et al. 2016). Each of

535   these approaches (PTV-X-ray combination, magnetic resonance and X-ray - numerical

536   simulation combination) has its own strengths and weaknesses with respect to spatial

537   resolution, accuracy and assumptions made concerning biofilm-flow coupling. The magnetic

538   resonance approach offers even finer ($< 50\ \mu$m) spatial resolution than the present approach

539   and does not require index matching or referencing between flow and biofilm data because all

540   phases are extracted from the same data set. However, it is not trivial to distinguish between

541   flow in pore spaces and fluid inside biofilms because biofilms tend to be permeable and the

542   magnetic resonance signal also captures flow inside the biofilm (e.g. Seymour et al. 2004).

543   Numerical simulations based on X-ray geometries offer very high resolution and accuracy.

544   However, assumptions must be made, for example, concerning the permeability of the biofilm

545   or biofilm growth (e.g. von Schulenburg et al. 2009, Bottero et al. 2013). There is therefore no

546   *best* approach but rather the optimal method should be chosen depending on the specific setup

547   and research goal in mind.

5. Conclusions

549   This study presents experimental measurements on porescale hydrodynamics, porespace

550   structure and biofilm morphology in a progressively bioclogged porous medium with the aim

551   of delineating the influence of the porespace geometry, wall shear stresses, and mass transfer

552   processes on biofilm growth. The local wall shear stress measurements revealed that the

553   attachment and development of biofilm patches was controlled by the local wall shear stress.

554   Biofilm formation occurred in the regions of low shear stresses, while no significant amount

555   of biofilm grew in the regions of high shear stresses. Biofilms were found at local wall shear

556   stresses up to 0.02 N, which defines a maximal shear strength of the biofilm in the porous

557   medium. Mass transfer processes played a secondary role for growth, consistent with presence

558   of nutrient and electron acceptors in excess in our experiments. The development of biofilm

559   substantially influenced the porescale hydrodynamics, as shown by the significant increase of

560   the pore velocities and wall shear stresses, both in terms of average value and variance. Given

561   that the flow rate was kept constant, the increase of average pore velocity is a consequence of

562   the porosity reduction upon biofilm growth. However, growth was not homogeneous in space

563   and resulted in the clogging of certain pores so that the pore scale flow arrangement changed

564   from a predominantly parallel configuration towards a more serial one. This is a manifestation

565   of the formation of preferential flow pathways in the bioclogged porous medium. We propose

566   that, based on this method, measured biofilm shear strength could be used to validate models

567   used in numerical simulations of biofilm growth in porous media. Furthermore, the growth

568   conditions used in the current study could be tailored to provide experimental data for

569   practical applications that seek to optimize biofilm thickness or specific surface area and that

570   upscale mass transfer processes to practically relevant scales of sand or trickling filters.

571   Finally, with the fast pace of development of 3D printing technology (in terms of printable

572   materials, geometries and scales accessible), the 3D printing of Nafion (James et al. 2015)

573   might soon allow similar investigations in other geometries (non-granular porous media,

574   membrane feed spacer channels) and at scales relevant for other practical applications.

587

588 **References:**

589 Griebler, C. and Lueders, T. (2009) Microbial biodiversity in groundwater ecosystems. Freshwater
590 Biology 54(4), 649-677.
591 Meckenstock, R.U., Elsner, M., Griebler, C., Lueders, T., Stumpp, C., Aamand, J., Agathos, S.N.,
592 Albrechtsen, H.-J., Bastiaens, L., Bjerg, P.L., Boon, N., Dejonghe, W., Huang, W.E., Schmidt, S.I.,
593 Smolders, E., Sørensen, S.R., Springael, D. and van Breukelen, B.M. (2015) Biodegradation: Updating
594 the Concepts of Control for Microbial Cleanup in Contaminated Aquifers. Environmental Science &
595 Technology 49(12), 7073-7081.
596 Gujer, W. and Boller, M. (1986) Design of a nitrifying tertiary trickling filter based on theoretical
597 concepts. Water Research 20(11), 1353-1362.
598 Morgenroth, E., Schroeder, E.D., Chang, D.P.Y. and Scow, K.M. (1996) Nutrient Limitation in a
599 Compost Biofilter Degrading Hexane. Journal of the Air & Waste Management Association 46(4), 300-
600 308.
601 Gülay, A., Tatari, K., Musovic, S., Mateiu, R.V., Albrechtsen, H.-J. and Smets, B.F. (2014) Internal
602 Porosity of Mineral Coating Supports Microbial Activity in Rapid Sand Filters for Groundwater
603 Treatment. Applied and Environmental Microbiology 80(22), 7010-7020.
604 Baker, J.S. and Dudley, L.Y. (1998) Biofouling in membrane systems — A review. Desalination 118(1),
605 81-89.
606 Eberl, H.J., Picioreanu, C., Heijnen, J.J. and van Loosdrecht, M.C.M. (2000) A three-dimensional
607 numerical study on the correlation of spatial structure, hydrodynamic conditions, and mass transfer
608 and conversion in biofilms. Chemical Engineering Science 55(24), 6209-6222.
609 Picioreanu, C., van Loosdrecht, M.C.M. and Heijnen, J.J. (2000) A theoretical study on the effect of
610 surface roughness on mass transport and transformation in biofilms. Biotechnology and
611 Bioengineering 68(4), 355-369.
612 Battin, T.J., Sloan, W.T., Kjelleberg, S., Daims, H., Head, I.M., Curtis, T.P. and Eberl, L. (2007) Microbial
613 landscapes: new paths to biofilm research. Nat Rev Micro 5(1), 76-81.
614 Rusconi, R., Guasto, J.S. and Stocker, R. (2014) Bacterial transport suppressed by fluid shear. Nat Phys
615 10(3), 212-217.
616 Radu, A., van Steen, M., Vrouwenvelder, J.S., van Loosdrecht, M. and Picioreanu, C. (2014) Spacer
617 geometry and particle deposition in spiral wound membrane feed channels. Water Research 64, 160-
618 176.
619 Seymour, J.D., Gage, J.P., Codd, S.L. and Gerlach, R. (2004) Anomalous Fluid Transport in Porous
620 Media Induced by Biofilm Growth. Physical Review Letters 93(19), 198103.
621 Holzner, M., Morales, V.L., Willmann, M. and Dentz, M. (2015) Intermittent Lagrangian velocities and
622 accelerations in three-dimensional porous medium flow. Physical Review E 92(1), 013015.
623 Bottero, S., Storck, T., Heimovaara, T.J., van Loosdrecht, M.C.M., Enzien, M.V. and Picioreanu, C.
624 (2013) Biofilm development and the dynamics of preferential flow paths in porous media. Biofouling.
625 Coyte, K.Z., Tabuteau, H., Gaffney, E.A., Foster, K.R. and Durham, W.M. (2017) Microbial competition
626 in porous environments can select against rapid biofilm growth. Proceedings of the National
627 Academy of Sciences 114(2), E161-E170.
628 Nadell, C.D., Ricaurte, D., Yan, J., Drescher, K. and Bassler, B.L. (2017) Flow environment and matrix
629 structure interact to determine spatial competition in Pseudomonas aeruginosa biofilms. eLife 6,
630 e21855.
631 Drescher, K., Shen, Y., Bassler, B.L. and Stone, H.A. (2013) Biofilm streamers cause catastrophic
632 disruption of flow with consequences for environmental and medical systems. Proceedings of the
633 National Academy of Sciences 110(11), 4345-4350.
634 Qian, J., Horn, H., Tarchitzky, J., Chen, Y., Katz, S. and Wagner, M. (2017) Water quality and daily
635 temperature cycle affect biofilm formation in drip irrigation devices revealed by optical coherence
636 tomography. Biofouling 33(3), 211-221.
637 Kapellos, G.E., Alexiou, T.S. and Payatakes, A.C. (2007) Hierarchical simulator of biofilm growth and
638 dynamics in granular porous materials. Advances in Water Resources 30(6–7), 1648-1667.

639 Xi, C., Marks, D., Schlachter, S., Luo, W. and Boppart, S.A. (2006) High-resolution three-dimensional
640 imaging of biofilm development using optical coherence tomography. Journal of Biomedical Optics
641 11(3), 034001-034001-034006.
642 Wagner, M., Taherzadeh, D., Haisch, C. and Horn, H. (2010a) Investigation of the mesoscale structure
643 and volumetric features of biofilms using optical coherence tomography. Biotechnology and
644 Bioengineering 107(5), 844-853.
645 Derlon, N., Peter-Varbanets, M., Scheidegger, A., Pronk, W. and Morgenroth, E. (2012) Predation
646 influences the structure of biofilm developed on ultrafiltration membranes. Water Research 46(10),
647 3323-3333.
648 Gao, Y., Haavisto, S., Li, W., Chuyang, T., Salmela, J. and Fane, A.G. (2014) A Novel Approach to
649 Characterizing the Growth of a Fouling Layer during Membrane Filtration via Optical Coherence
650 Tomography. Environmental Science & Technology.
651 Weiss, N., van Leeuwen, T.G. and Kalkman, J. (2015) Simultaneous and localized measurement of
652 diffusion and flow using optical coherence tomography. Optics Express 23(3), 3448-3459.
653 Codd, S.L., Vogt, S.J., Hornemann, J.A., Phillips, A.J., Maneval, J.E., Romanenko, K.R., Hansen, L.,
654 Cunningham, A.B. and Seymour, J.D. (2011) NMR relaxation measurements of biofouling in model
655 and geological porous media. Organic Geochemistry 42(8), 965-971.
656 Wagner, M., Manz, B., Volke, F., Neu, T.R. and Horn, H. (2010b) Online assessment of biofilm
657 development, sloughing and forced detachment in tube reactor by means of magnetic resonance
658 microscopy. Biotechnology and Bioengineering 107(1), 172-181.
659 Stewart, P.S. (2014) Biophysics of biofilm infection. Pathogens and Disease 70(3), 212-218.
660 Stewart, P.S. and Franklin, M.J. (2008) Physiological heterogeneity in biofilms. Nat Rev Micro 6(3),
661 199-210.
662 Derlon, N., Massé, A., Escudié, R., Bernet, N. and Paul, E. (2008) Stratification in the cohesion of
663 biofilms grown under various environmental conditions. Water Research 42(8–9), 2102-2110.
664 Blauert, F., Horn, H. and Wagner, M. (2015) Time-resolved biofilm deformation measurements using
665 optical coherence tomography. Biotechnology and Bioengineering 112(9), 1893-1905.
666 Downie, H., Holden, N., Otten, W., Spiers, A.J., Valentine, T.A. and Dupuy, L.X. (2012) Transparent Soil
667 for Imaging the Rhizosphere. PLoS ONE 7(9), e44276.
668 Desmond, P., Best, J.P., Morgenroth, E. and Derlon, N. (2018) Linking composition of extracellular
669 polymeric substances (EPS) to the physical structure and hydraulic resistance of membrane biofilms.
670 Water Research 132, 211-221.
671 Hoyer, K., Holzner, M., Lüthi, B., Guala, M., Liberzon, A. and Kinzelbach, W. (2005) 3D scanning
672 particle tracking velocimetry. Experiments in Fluids 39(5), 923-934.
673 Davit, Y., Iltis, G., Debenest, G., Veran-Tissoires, S., Wildenschild, D., Gerino, M. and Quintard, M.
674 (2011) Imaging biofilm in porous media using X-ray computed microtomography. Journal of
675 Microscopy 242(1), 15-25.
676 Carrel, M., Beltran, M.A., Morales, V.L., Derlon, N., Morgenroth, E., Kaufmann, R. and Holzner, M.
677 (2017) Biofilm imaging in porous media by laboratory X-Ray tomography: Combining a non-
678 destructive contrast agent with propagation-based phase-contrast imaging tools. PLoS ONE 12(7),
679 e0180374.
680 Schindelin, J., Arganda-Carreras, I., Frise, E., Kaynig, V., Longair, M., Pietzsch, T., Preibisch, S., Rueden,
681 C., Saalfeld, S., Schmid, B., Tinevez, J.-Y., White, D.J., Hartenstein, V., Eliceiri, K., Tomancak, P. and
682 Cardona, A. (2012) Fiji: an open-source platform for biological-image analysis. Nature Methods 9,
683 676.
684 Pérez-Reche, F.J., Taraskin, S.N., Otten, W., Viana, M.P., Costa, L.d.F. and Gilligan, C.A. (2012)
685 Prominent Effect of Soil Network Heterogeneity on Microbial Invasion. Physical Review Letters
686 109(9), 098102.
687 de Anna, P., Quaife, B., Biros, G. and Juanes, R. (2017) Prediction of the low-velocity distribution from
688 the pore structure in simple porous media. Physical Review Fluids 2(12), 124103.
689 Davit, Y., Byrne, H., Osborne, J., Pitt-Francis, J., Gavaghan, D. and Quintard, M. (2013) Hydrodynamic
690 dispersion within porous biofilms. Physical Review E 87(1), 012718.

691 Stoodley, P., deBeer, D. and Lewandowski, Z. (1994) Liquid Flow in Biofilm Systems. Applied and
692 Environmental Microbiology 60(8), 2711-2716.
693 Deng, W., Cardenas, M.B., Kirk, M.F., Altman, S.J. and Bennett, P.C. (2013) Effect of Permeable
694 Biofilm on Micro- And Macro-Scale Flow and Transport in Bioclogged Pores. Environmental Science &
695 Technology 47(19), 11092-11098.
696 de Anna, P., Le Borgne, T., Dentz, M., Tartakovsky, A.M., Bolster, D. and Davy, P. (2013) Flow
697 Intermittency, Dispersion, and Correlated Continuous Time Random Walks in Porous Media. Physical
698 Review Letters 110(18), 184502.
699 Morales, V.L., Dentz, M., Willmann, M. and Holzner, M. (2017) Stochastic dynamics of intermittent
700 pore-scale particle motion in three–dimensional porous media: Experiments and theory. Geophysical
701 Research Letters, n/a-n/a.
702 Siena, M., Riva, M., Hyman, J.D., Winter, C.L. and Guadagnini, A. (2014) Relationship between pore
703 size and velocity probability distributions in stochastically generated porous media. Physical Review E
704 89(1), 013018.
705 Horn, H. and Lackner, S. (2014) Productive Biofilms. Muffler, K. and Ulber, R. (eds), pp. 53-76,
706 Springer International Publishing, Cham.
707 Thullner, M. and Baveye, P. (2008) Computational pore network modeling of the influence of biofilm
708 permeability on bioclogging in porous media. Biotechnology and Bioengineering 99(6), 1337-1351.
709 Song, J.L., Au, K.H., Huynh, K.T. and Packman, A.I. (2014) Biofilm responses to smooth flow fields and
710 chemical gradients in novel microfluidic flow cells. Biotechnology and Bioengineering 111(3), 597-
711 607.
712 Möhle, R.B., Langemann, T., Haesner, M., Augustin, W., Scholl, S., Neu, T.R., Hempel, D.C. and Horn,
713 H. (2007) Structure and shear strength of microbial biofilms as determined with confocal laser
714 scanning microscopy and fluid dynamic gauging using a novel rotating disc biofilm reactor.
715 Biotechnology and Bioengineering 98(4), 747-755.
716 Pintelon, T.R.R., Picioreanu, C., van Loosdrecht, M.C.M. and Johns, M.L. (2012) The effect of biofilm
717 permeability on bio-clogging of porous media. Biotechnology and Bioengineering 109(4), 1031-1042.
718 Peszynska, M., Trykozko, A., Iltis, G., Schlueter, S. and Wildenschild, D. (2016) Biofilm growth in
719 porous media: experiments, computational modeling at the porescale, and upscaling. Advances in
720 Water Resources 95, 288-301.

721

722

723 **List of tables:**

724 **Table 1**

725

726 **Table 1:** Average and maximal values of the wall shear stress measured at the location of the
727 nascent biofilm and at the surface of the biofilm as well as at the surface of the solid grains at
728 the start and end of the experiment. The distinction was here performed by considering the
729 data in one radius distance of the solid (Nafion grains (N) or biofilm (BF) faces). I_F stands for
730 the increase factor between the initial corresponding value and the value obtained after
731 biofilm growth.

	$<\tau_w>$ (N/m^2)			max(τ_w) (N/m^2)		
	T = 0 h	T = 36 h	I_F	T = 0 h	T = 36 h	I_F
BF	0.0037	0.0067	1.8	0.0152	0.0214	1.4
N	0.0065	0.0129	1.9	0.0391	0.0981	2.5

732

733

734

735

736

737

738

739

740 **List of figures:**

741 **Figure 1**

742 **Figure 2**

743 **Figure 3**

744 **Figure 4**
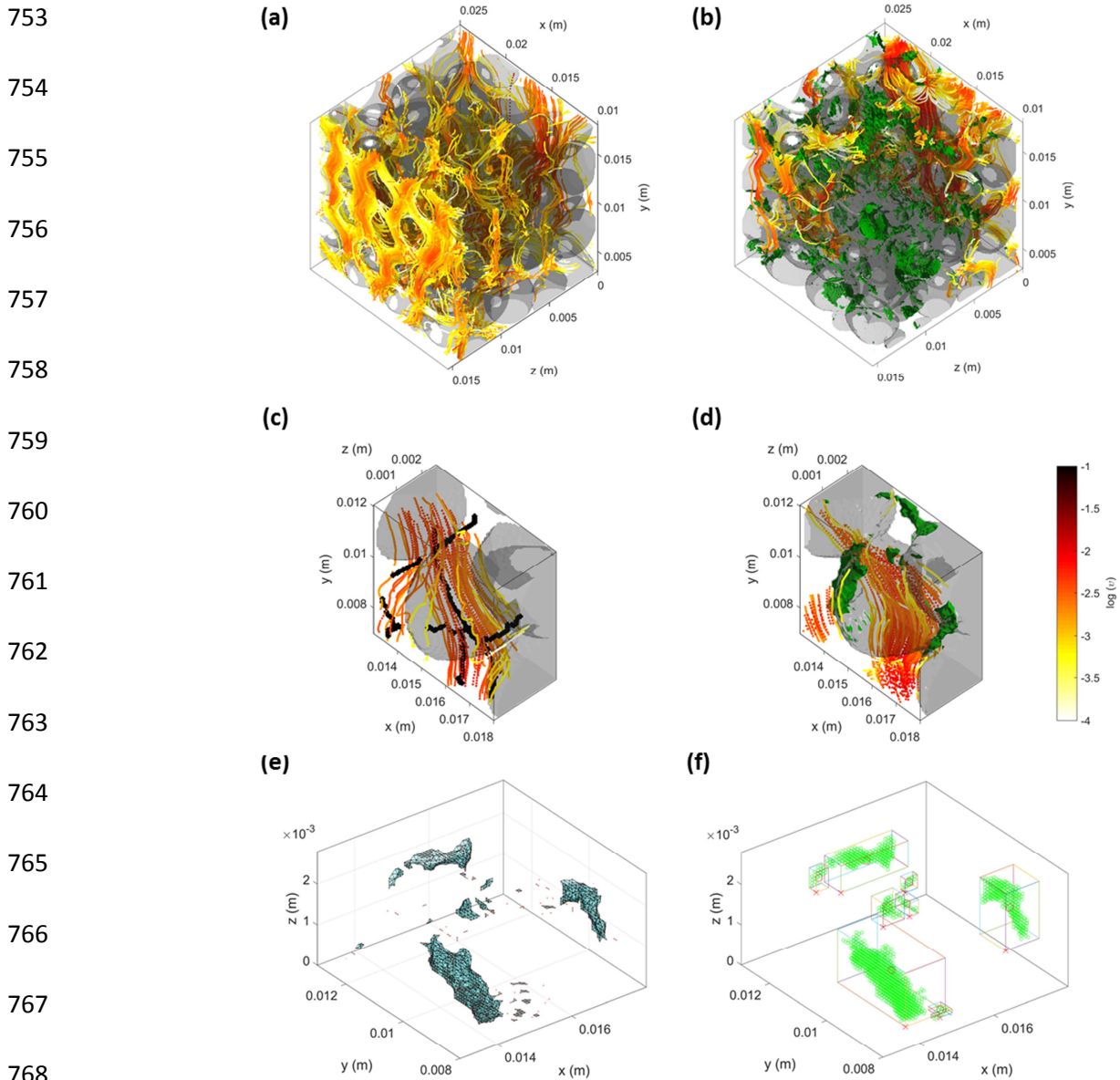
745 **Figure 5**

746 **Figure 6**

747 **Figure 7**

748

749

(a)

Bubble Trap
Peristaltic Pump
Flow Cell
Waste
Feed Solution

(b)

Waste
Flow Cell
Bubble Trap
Image Splitter
Syringe Pump
Laser
Camera
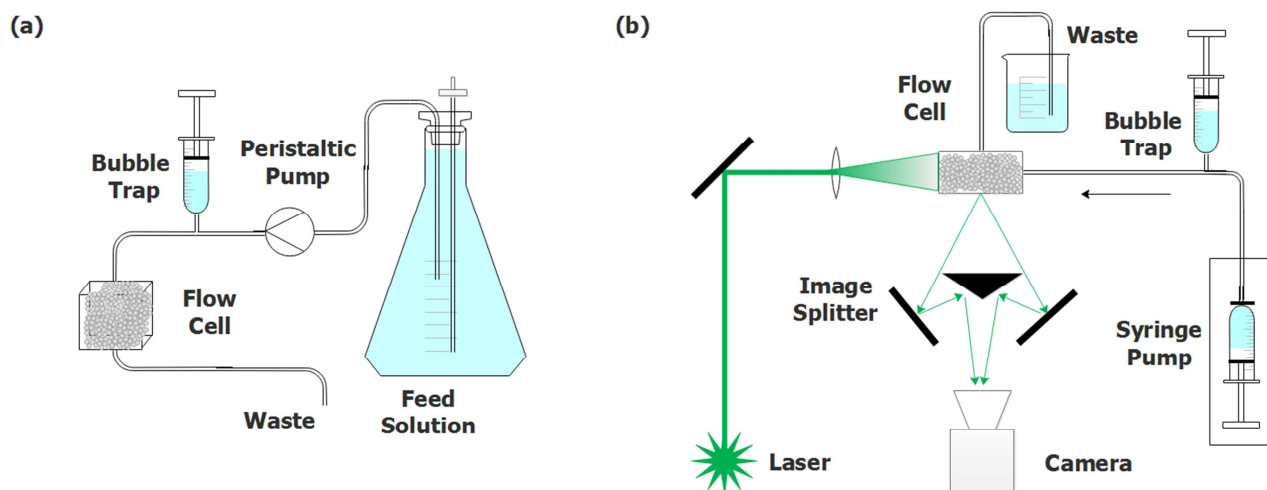
750   **Figure 1:** Schematics of the set up used (a) for biofilm cultivation and (b) for the 3D-PTV

751   measurements.

752

Figure 2: Registered 3D-PTV and X-ray data of the central zone for the clean (a) and bioclogged (b) porous medium. The solid surfaces (Nafion grains and biofilm) represent a color-coded (Nafion grains in grey and biofilm in green) Delaunay triangulation of the segmented X-ray data. (c) and (d) show a local magnification of a pore before and after biofilm colonization. Black lines in (c) represent the skeleton along which the pore radii were computed. The colorbar in (d) shows the scale of the velocity magnitude used for (a)-(d). The pore skeleton is not shown in (a), (b) and (d) for the sake of clarity. (e) shows the biofilm patches illustrated in (d). (f) shows the same patches and bounding boxes from which the aspect ratio of the patches were computed. Objects smaller than 10 voxels visible in (e) are removed in (f).
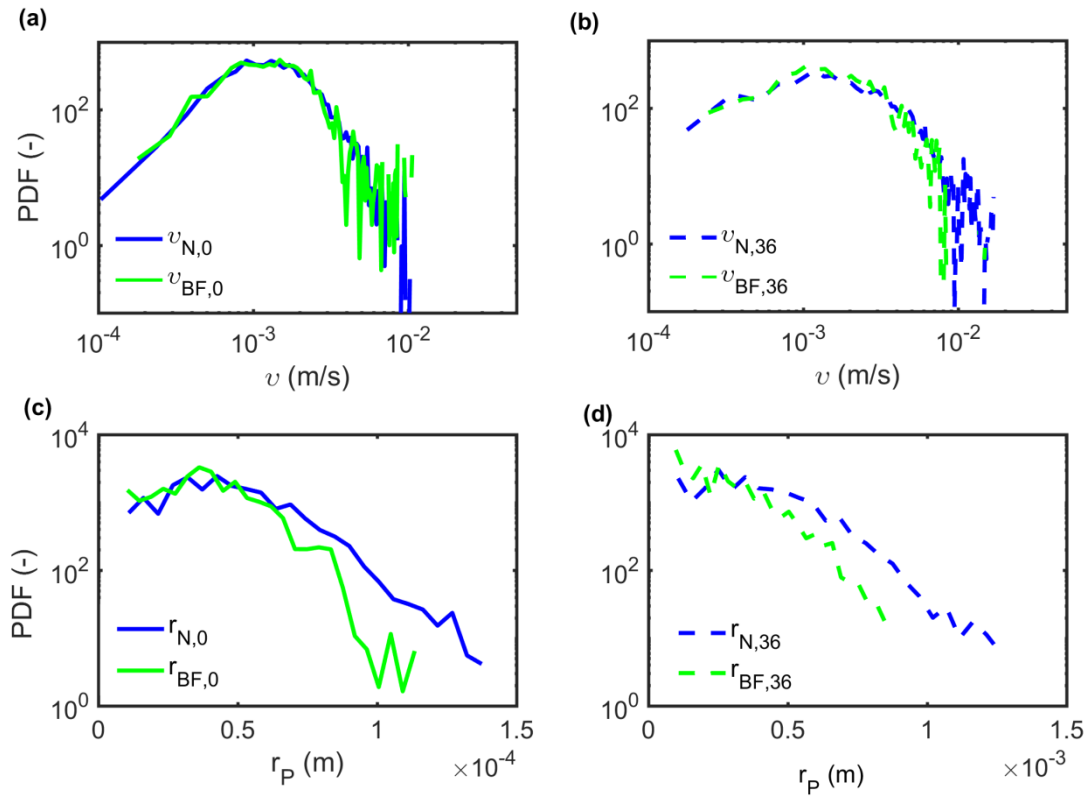
33

779
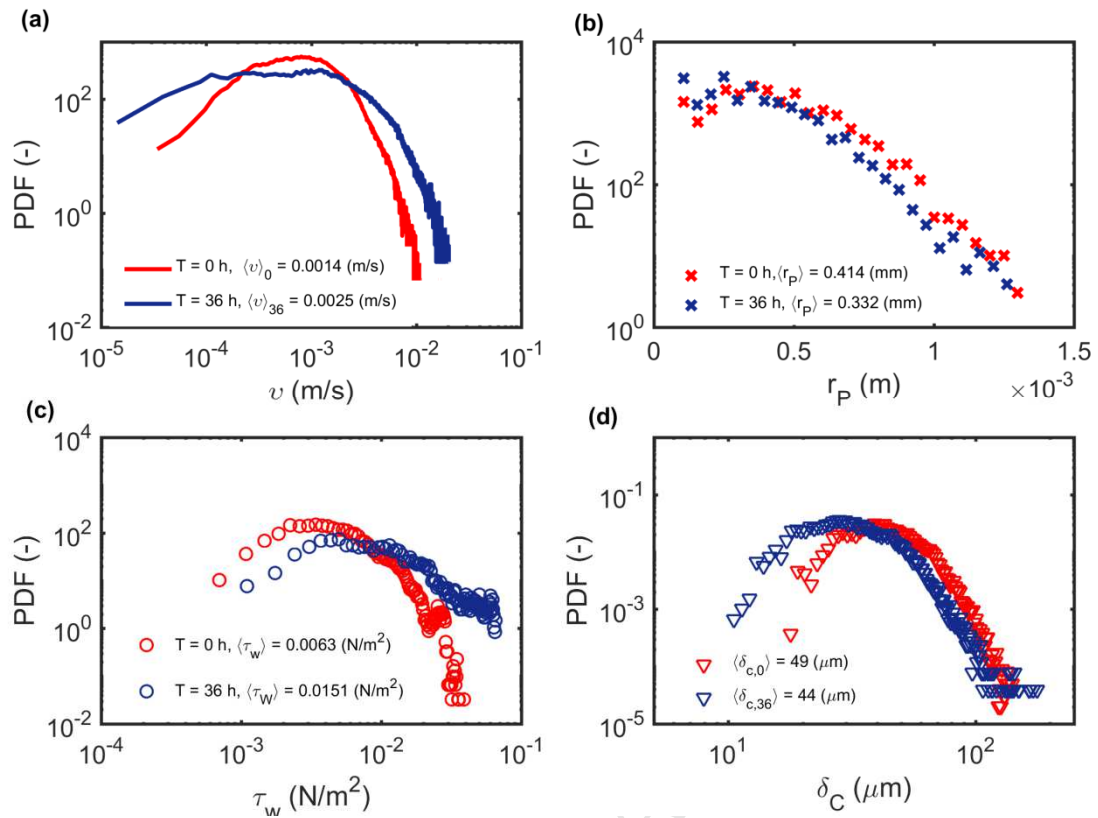
Figure 3: Probability density functions of the velocity magnitude (a), pore radii (b), wall

shear stresses (c), and of concentration boundary layer thicknesses (d) for the two different

time points during biofilm growth: clean (T = 0hr) and bioclogged porous media (T = 36 h).

Angular brackets denote the average over all measured values.

784

785

786

787

788
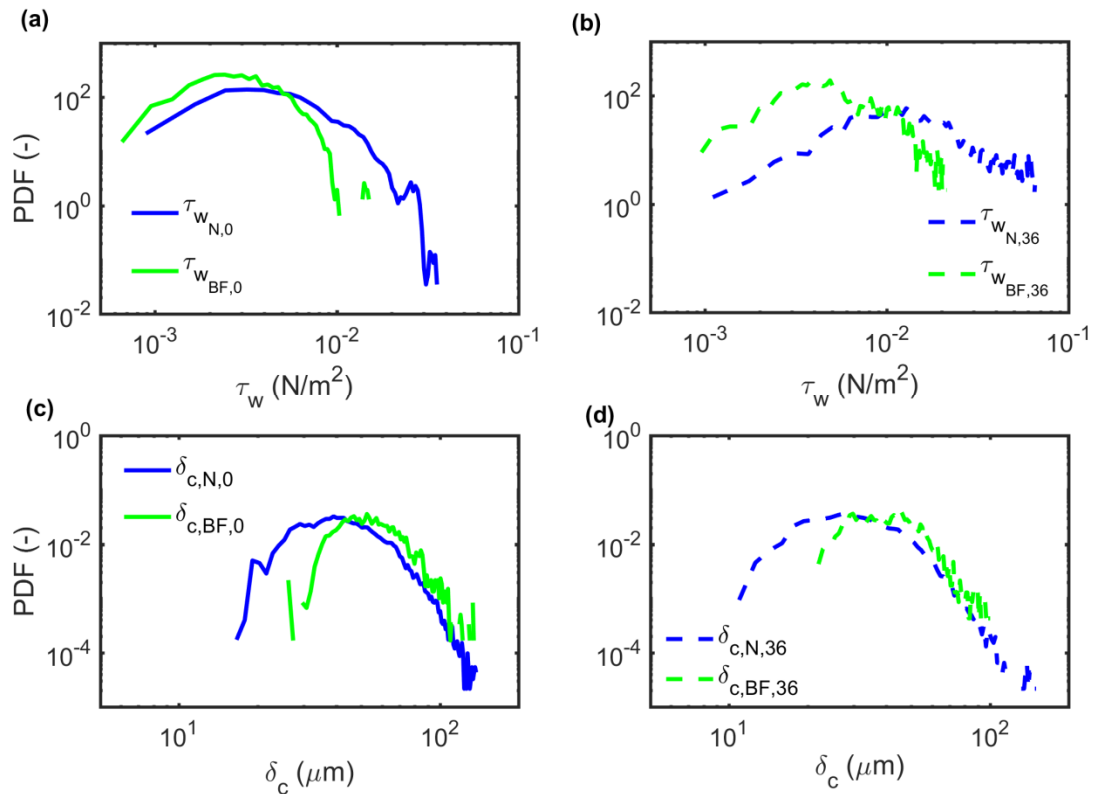
Figure 4: (a) and (b) show the PDFs of the pore-scale velocity magnitudes for the clean and bioclogged porous medium, whereas (c) and (d) show the corresponding pore radii PDFs. . "BF" and "N" here indicates if the considered data is located within a distance of one pore radius to the biofilm or uncolonized Nafion grains, respectively.

793
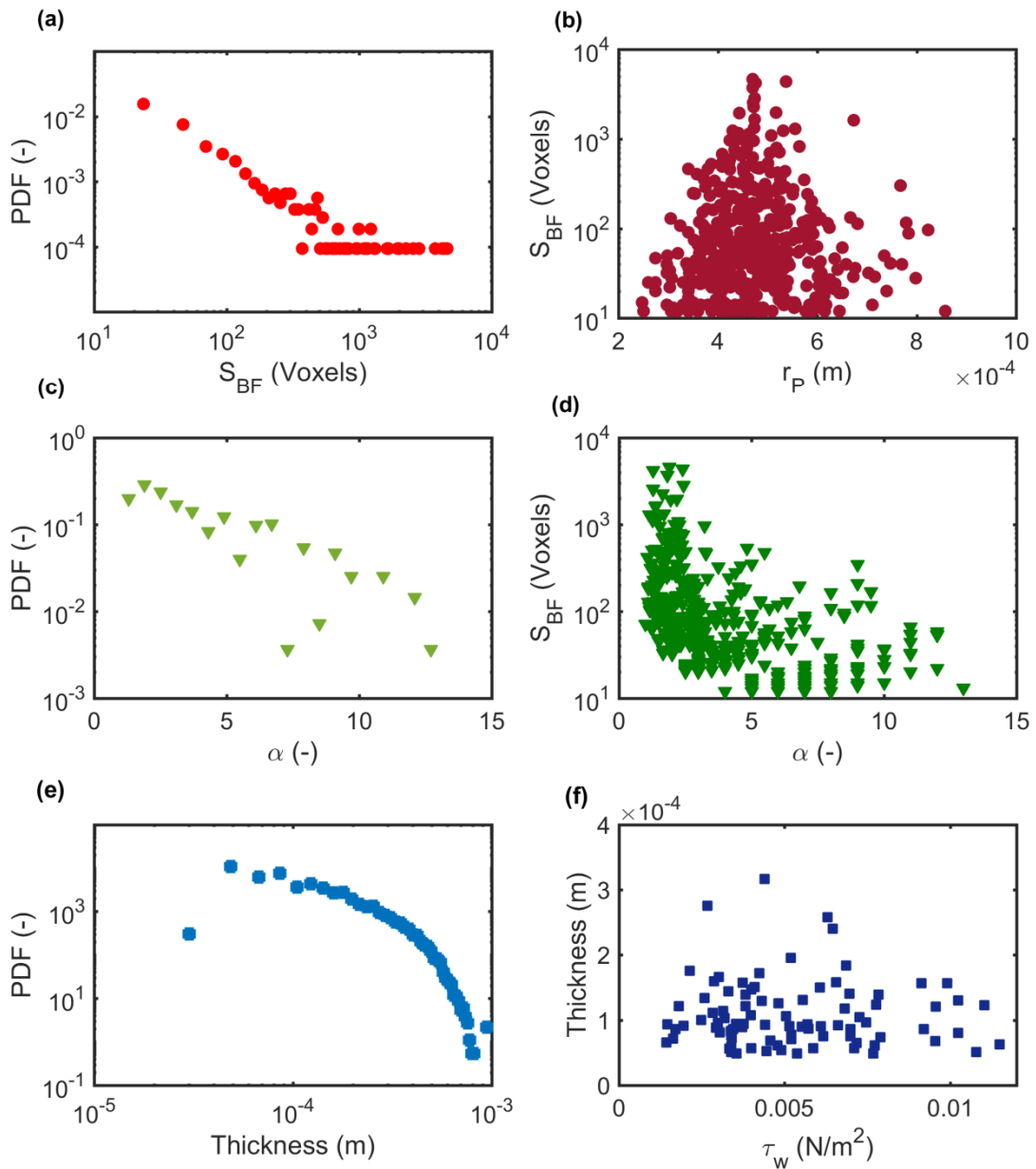
794

Figure 5: PDFs of the pore-scale velocity magnitudes for the clean (a) and bioclogged (b)

porous medium. Concentration boundary layer thickness PDFs for the clean (c) and

bioclogged (d) porous medium. "BF" and "N" here indicates if the considered data is located

within a distance of one pore radius to the biofilm or uncolonized Nafion grains, respectively.

799

Figure 6: (a) PDF of the biofilm patch size (S_{BF}) and (b) correlation of biofilm patch sizes with average pore radii. (c) PDF of biofilm patch aspect ratio (α) and (d) correlation of biofilm patch size with aspect ratio. (e) PDF of the biofilm thickness and(f) correlation of biofilm thickness with wall shear stress.

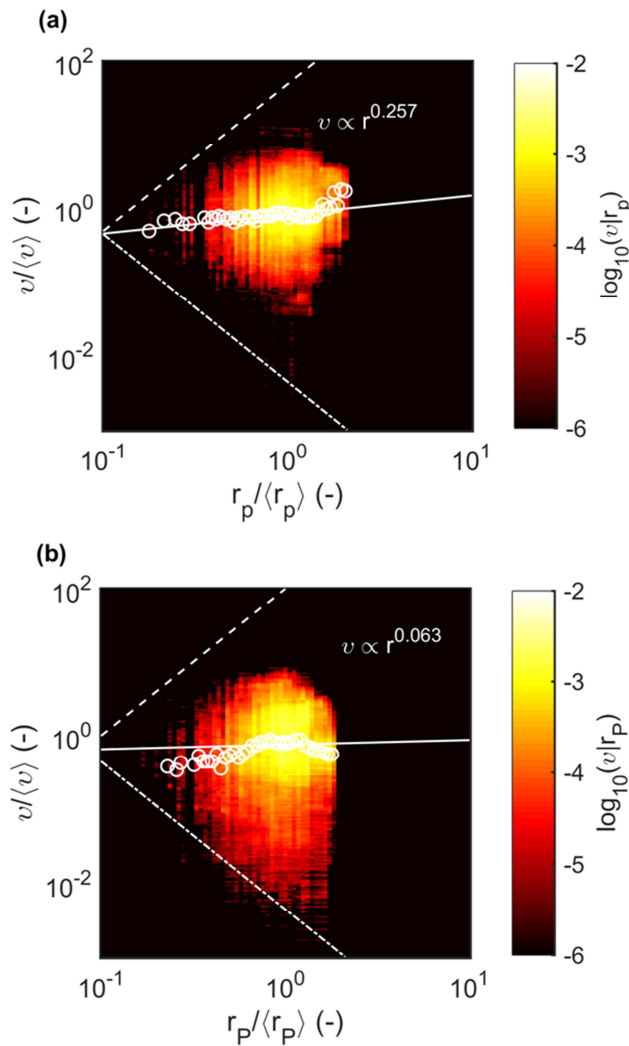807
808
809
810
811
812
813
814
815
816
817
818
819
820
821
822
823
824
825
826

Figure 7: Joint PDFs of $v/\langle v \rangle$ and $r_P/\langle r_P \rangle$ for the clean (a) and bioclogged (b) porous media. The dashed and dashed-dotted lines show power laws with exponents of 2 and -2, respectively. The white circles are conditional averages of $v/\langle v \rangle$ and $r_P/\langle r_P \rangle$ and the continuous line is a power function fitted to the conditional average. The exponents of the power function are indicated as imbedded text.

Highlights:

- Influence of shear and mass transfer on biofilm growth in porous media is studied

- Wide distributions of wall shear stresses and CBL thicknesses measured

- The wall shear stress controls biofilm initial attachment and growth

- Our method allows estimating the biofilm shear for a substratum of complex geometry

- Biofilm growth induces complex changes in the 3D pore-scale hydrodynamics